



저작자표시-비영리-변경금지 2.0 대한민국

이용자는 아래의 조건을 따르는 경우에 한하여 자유롭게

- 이 저작물을 복제, 배포, 전송, 전시, 공연 및 방송할 수 있습니다.

다음과 같은 조건을 따라야 합니다:



저작자표시. 귀하는 원저작자를 표시하여야 합니다.



비영리. 귀하는 이 저작물을 영리 목적으로 이용할 수 없습니다.



변경금지. 귀하는 이 저작물을 개작, 변형 또는 가공할 수 없습니다.

- 귀하는, 이 저작물의 재이용이나 배포의 경우, 이 저작물에 적용된 이용허락조건을 명확하게 나타내어야 합니다.
- 저작권자로부터 별도의 허가를 받으면 이러한 조건들은 적용되지 않습니다.

저작권법에 따른 이용자의 권리는 위의 내용에 의하여 영향을 받지 않습니다.

이것은 [이용허락규약\(Legal Code\)](#)을 이해하기 쉽게 요약한 것입니다.

[Disclaimer](#)

공학석사 학위논문

**Improved Performance of
Mn₃O₄ Nanoparticles
on Nitrogen-doped Graphene for
Lithium Ion Battery Anodes**

**질소 도핑된 그래핀에 담지를 통한
Mn₃O₄ 나노입자의 리튬이온전지
음극소재로서의 성능 향상**

2014년 2월

서울대학교 대학원

공과대학 화학생명공학부

Jin Aihua

**Improved Performance of
Mn₃O₄ Nanoparticles
on Nitrogen-doped Graphene for
Lithium Ion Battery Anodes**

지도 교수 성 영 은

**이 논문을 공학석사 학위논문으로 제출함
2013 년 12 월**

**서울대학교 대학원
공과대학 화학생명공학부
Jin Aihua**

**Jin Aihua의 석사 학위논문을 인준함
2013 년 12 월.**

위 원 장 _____ (인)

부위원장 _____ (인)

위 원 _____ (인)

Abstract

Improved Performance of Mn_3O_4 Nanoparticles on Nitrogen-doped Graphene for Lithium Ion Battery Anodes

Jin Aihua

School of Chemical & Biological Engineering

Seoul National University

Lithium ion batteries (LIBs) have been widely applied as major power sources for electronic devices. To utilize lithium ion battery to electric vehicles, plenty of research is going on. Developing new electrode materials with high specific capacity for excellent lithium ion storage properties is very desirable.

In this research, a simple hydrothermal method for the growth of Mn_3O_4 nanoparticles onto nitrogen-doped graphene (N-doped graphene) for high-performance lithium ion battery (LIB) anodes is introduced. Hydrazine plays a fundamental role in the formation of such nanostructures as it can act both as a reducing agent and as a nitrogen source. In the synthesized composite, highly crystalline Mn_3O_4 nanoparticles with average sizes of 20–50 nm are

homogeneously dispersed on both sides of the N-doped graphene. The nitrogen content in the doped graphene is confirmed by elemental analyzer, and 2 wt% of the sample is found to be composed of nitrogen element. The as-prepared Mn₃O₄/N-doped graphene composites exhibit remarkable electrochemical performance, including high reversible specific capacity, outstanding cycling stability, and excellent rate capability (approximately 400 mA h g⁻¹ at 2.0 A g⁻¹) when used as the anode material for LIBs. The improvement in the electrochemical properties of the material can be attributed to graphene, which acts as both an electron conductor and a volume buffer layer, and nitrogen doping allows for fast electron and ion transfer by decreasing the energy barrier. This type of metal oxide/N-doped graphene composites can be promising candidates for high-performance anode materials for LIBs.

Keywords: Lithium ion batteries, anode, manganese oxide, graphene, doping

Student Number: 2012-22575

Contents

Chapter 1. Introduction	1
Chapter 2. Background.....	6
2.1 The mechanisms of LIBs.....	6
2.2 Components in LIBs	8
2.2.1 Cathode	8
2.2.2 Anode	12
2.2.3 Electrolyte	18
Chapter 3. Experimental	20
3.1 Preparation of materials	20
3.2 Preparation of composite electrode	21
3.3 Preparation of half cell	22
3.4 Characterization	22
3.5 Electrochemical measurement	23
Chapter 4 Results and discussion	24
4.1 The analysis of powder	24
4.2 The electrochemical analysis	37
Chapter 5 Conclusions	50
References	51
국문초록.....	58

List of Figures

- Figure 2.1** Schematic illustration of the lithium ion battery.....7
- Figure 2.2** Schematic crystal structures of three types of cathode materials: (a) LiCoO_2 , (b) LiMn_2O_4 , (C) LiFePO_411
- Figure 2.3** A schematic representation of the different reaction mechanisms observed in electrode materials for lithium batteries. Black circles: voids in the crystal structure, blue circles: metal, yellow circles: lithium.....14
- Figure 2.4** Gravimetric and volumetric capacities for selected alloying reactions. Capacities for graphite are given as references.....15
- Figure 2.5** Theoretical (black bars), first discharge (dark grey), and charge (light grey) specific gravimetric capacities of different compounds that react with lithium through a conversion reaction.....17
- Figure 4.1** (a, b) SEM images and (c, d) TEM images of M-NG composite (inset : HR-TEM image of Mn_3O_4 nanoparticle on the graphene sheet)26
- Figure 4.2** SEM images of M-G composite27
- Figure 4.3** SEM and TEM images of bare Mn_3O_4 nanoparticles...28

Figure 4.4	(a) XRD patterns of GO, NG and M-NG composite, (b) TGA curve of M-NG composite.....	30
Figure 4.5	Raman spectra of GO, NG, bare Mn ₃ O ₄ and M-NG composite.....	33
Figure 4.6	XPS spectra of the (a) C 1s region of GO, (b) C 1s region, (c) Mn 2p region, and (d) N 1s region of M-NG composite.....	34
Figure 4.7	Voltage profiles of (a) M-NG composite and (b) M-G composite and (c) bare Mn ₃ O ₄ and (d) Cyclic voltammograms of M-NG composite at a scanning rate of 0.1 mV s ⁻¹	40
Figure 4.8	(a) Cycle performances of M-NG composite (squares, red), M-G composite (triangle, dark yellow) and bare Mn ₃ O ₄ (circles, blue) at a current density of 200 mA g ⁻¹ (b) Rate properties of M-NG composite (squares, red), M-G composite (triangle, dark yellow) and bare Mn ₃ O ₄ (circles, blue).....	43
Figure 4.9	Cycle performances of G and NG cycled at 200 mA g ⁻¹ for 40 cycles.....	45
Figure 4.10	Nyquist plots of the M-NG composite and bare Mn ₃ O ₄ at the charged state after 1 cycle.....	47

Figure 4.11 HR TEM images of (a) M-NG and (b) bare Mn_3O_4 nanoparticles after 30 cycles at 200 mA g^{-1} 49

List of Tables

Table 1. Composition (wt%) of the GO, NG, M-NG and Mn ₃ O ₄ resulted from elemental analyzer.....	35
--	----

Chapter 1. Introduction

Efficient energy storage devices with an extended lifetime are required to meet the increasing energy demands in various fields such as electronics, as well as for renewable energy generation systems and electric vehicles. Lithium ion batteries (LIBs) have attracted great attention as one of the most dominant power sources because of their high power and energy densities [1, 2]. To meet the social demands associated with the use of LIBs in hybrid electric vehicles (HEVs), plug-in hybrid electric vehicles (PHEVs) and electric vehicles (EVs), considerable efforts are focused on improving their power and energy densities by exploring new electrode materials.

The first lithium ion battery was firstly introduced by Exxon in 1972. In this system, they used Li/TiS_2 as the negative and positive electrode, respectively, while firstly using lithium perchlorate in dioxolane as electrolyte [3]. Metallic lithium has many advantages including low redox potential and low weight. Nevertheless, lithium metal/liquid electrolyte combination can result in dendrite formations which finally lead to explosion hazards. In order to replace lithium metal, many anode materials have been developed. The problem seems solved when substituting lithium metal for lithium-aluminum

alloy, but it can only endure a short cycle life owing to volume changes.

Rachid Yazami demonstrated graphite intercalated compound by using graphite as anode in 1980. Sony Corporation commercialized the first non-aqueous LIBs in 1991 by applying graphite as anode and lithium transition metal oxides as cathode. Until now, graphitic materials are still commonly used as anodes in commercial LIBs due to their low cost, high electronic conductivity and cyclic stability [4-6]. However, graphite already approaches very close to the limited theoretical capacity (372 mA h g^{-1}) and graphite cannot satisfy the demand of high capacity storage [7]. Therefore, many studies are focused on improving the specific capacity of LIB anode materials [8-10].

Some transition-metal oxides such as Fe_2O_3 , Co_3O_4 , and Mn_3O_4 have been studied for use as anode materials because of their high specific capacity [11-13]. For example, Kim et al. have reported that uniform hematite nanocapsules exhibited a specific capacity of 740 mA h g^{-1} after 30 cycles, as well as excellent rate capability [11]. Moreover, Xiao et al. demonstrated that shape-controlled Co_3O_4 particles showed excellent lithium storage properties and cycling stability [12]. Among the transition-metal oxides, manganese oxide is

an interesting material because of its natural abundance, low toxicity, and low price. Furthermore, the theoretical specific capacity of Mn_3O_4 is about 937 mA h g^{-1} , which is almost three times greater than that of graphite. Nonetheless, the intrinsic low electrical conductivity ($\sim 10^{-7}$ – $10^{-8} \text{ S cm}^{-1}$) of this oxide highly limits its ubiquitous application in LIBs [14, 15]. To overcome this problem, conductive carbon/manganese oxide composites have been used, as this helps enhance the mechanical properties and electrical conductivity of manganese oxide as an electrode [16-18]. In this sense, Zhang and coworkers reported the use of manganese oxide nanoparticle loaded porous carbon nanofibers as anode materials. Because carbon nanofibers can act as a buffer to alleviate the large volume change of manganese oxide, the aforementioned structures exhibited superior reversible capacity and stable cycling performance [16]. Ajayan's group also reported coaxial manganese oxide/carbon nanotube arrays that showed excellent cyclic stability and capacity because of the improved electronic conductivity and a proposed dual mechanism of lithium storage [18].

Among the various conductive carbon materials, graphene has awakened a tremendous interest because of its very large theoretical specific surface area ($\sim 2600 \text{ m}^2 \text{ g}^{-1}$), superior electronic conductivity,

and physicochemical stability [19-21]. These unique properties make graphene a very promising electrode material for rechargeable LIBs. Actually, many groups have reported graphene-based anode materials with high specific capacity and superior cycle stability [22-32]. However, graphene shows rapid capacity fade during cycling, similar to other pure carbon nanomaterials [33].

Nitrogen doping of carbonaceous materials has been studied as an effective way to overcome the abovementioned limitations and improve the electrochemical performance. In particular, nitrogen doping of graphene-based materials allows for enhanced interaction with lithium ions and the creation of a greater number of active sites through modulation of the band structure of graphene [34, 35]. Indeed, these materials have shown enhanced cycling stability and rate performance in rechargeable LIBs [36, 37]. However, very few studies have been carried out on the use of nitrogen-doped graphene/manganese oxide composite as the LIB anode material.

Herein, we introduce a facile one-pot synthesis of Mn_3O_4 nanoparticle-nitrogen doped graphene nanocomposites (M-NG) based on a hydrazine-assisted hydrothermal method. In these composites, graphene serves both as a buffer and as an electron conductor, and nitrogen doping facilitates fast electron and ion transfer, leading to

high overall electrochemical performance. Compared to the previous reports, our method provides a simple way to prepare nitrogen-doped graphene/manganese oxide composites without high temperature and ammonia gas. Furthermore, these composites showed the improved electrochemical performance than un-doped graphene/Mn₃O₄ composites. From a practical vein, our strategy affords highly crystalline metal oxide nanoparticles embedded in a nitrogen-doped graphene matrix, which can greatly improve the electrochemical properties of LIBs.

Chapter 2. Background

2.1 The mechanisms of LIBs

Batteries consist of a series of electrochemical cells which can store energy in a form that can be converted to electrical energy. In many existing batteries, LIBs are one of the most popular rechargeable batteries that consist of cathode, anode and electrolyte separated by a separator. Copper and aluminum are used as current collectors for anode and cathode, respectively.

LIBs occur by oxidation and reduction reaction. During the charge process, oxidation reaction occurs on the cathode. Lithium ions are extracted from cathode and intercalate to anode by being supplied external energy. At the same time, electrons are transferred from cathode to anode through an external circuit. The opposite reaction happens during the discharge process. The mechanism of the lithium ion battery is shown in Fig. 2.1.

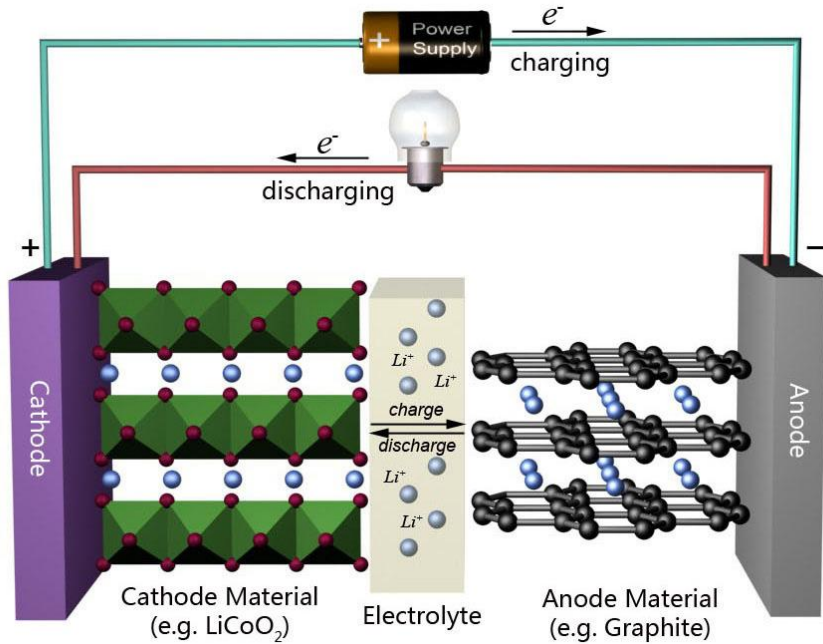


Fig. 2.1 Schematic illustration of the lithium ion battery. Adapted from Ref [38] (R. Liu, J. Duay and S. B. Lee, *Chem. Commun.*, 2011, **47**, 1384)

2.2 The components of LIBs

2.2.1 Cathode

In general, cathode materials should have high operating voltage, high energy density, high rate characteristics, good cycleability and small volume change. Otherwise, they also need to be chemically stable, nontoxic and inexpensive. The cathode materials currently being used can be classified into three types of metal oxides: layered oxides with α - NaFeO_2 , spinel and polyanion oxides with olivine structures (Fig 2.2) [39].

Among many cathode materials, LiCoO_2 is the most commonly used cathode material which forms the layered oxides with α - NaFeO_2 structure, which has the open structure where Li layer and Co layer are alternately ranged. With this structure, planes of Li ions through which lithiation and delithiation can occur. LiCoO_2 is developed by Goodenough group, which operate at high potential and wide temperature range, allows fast lithium ion diffusion, and has good life span. In general, operation potential of LiCoO_2 is restricted to 4.2 V (vs. Li/Li^+) and real specific capacity for 130 mAh g^{-1} [40, 41].

LiNiO_2 which has same structure with LiCoO_2 , has been proposed to replace LiCoO_2 due to its high price of Co and toxicity. LiNiO_2 is expected as the large capacity cathode materials because it

has 20~30% more amounts of reversibly reactive Li ion. However, in synthesis process, O_2 partial pressure should be increased because Ni replace with Li in the Li layer according to the instability of Ni^{2+} . Furthermore, the reproducibility of synthesis is unobtainable. In order to solve the limitations, the solid solution of $LiNiO_2$ and $LiCoO_2$ has been proposed and by this way can get specific capacity about 150 mAh g^{-1} . When compared with $LiCoO_2$, the discharge potential is slightly decreased [42, 43].

$LiMn_2O_4$, which has the spinel structure is an alternative. The specific capacity of this material is 100-120 mAh g^{-1} , which is 10% lower than $LiCoO_2$, however, attracts the attention due to simple synthesis process, good stability, and inexpensive price [44]. The reason it shows lower specific capacity is the plateau at 3.7 V. It is closely related with lithium accommodation lead to capacity decrease which caused by asymmetric lattice expansion/contraction of the electrode during cycling, generally from Jahn-Teller distortion of the Mn^{3+} ion. Generally, the critical reason of the cell degradation is the dissolution of Mn^{3+} [45].

$LiFePO_4$, which was suggested by Padhi et al., has brought a big attention to battery market. $LiFePO_4$ not only has a unique structure, but also Fe is natural abundant element, low cost and environmental

friendliness. This material's operating potential at 3.4 V (vs. Li/Li⁺) with good cycleability and high capacity about 170 mAh g⁻¹.

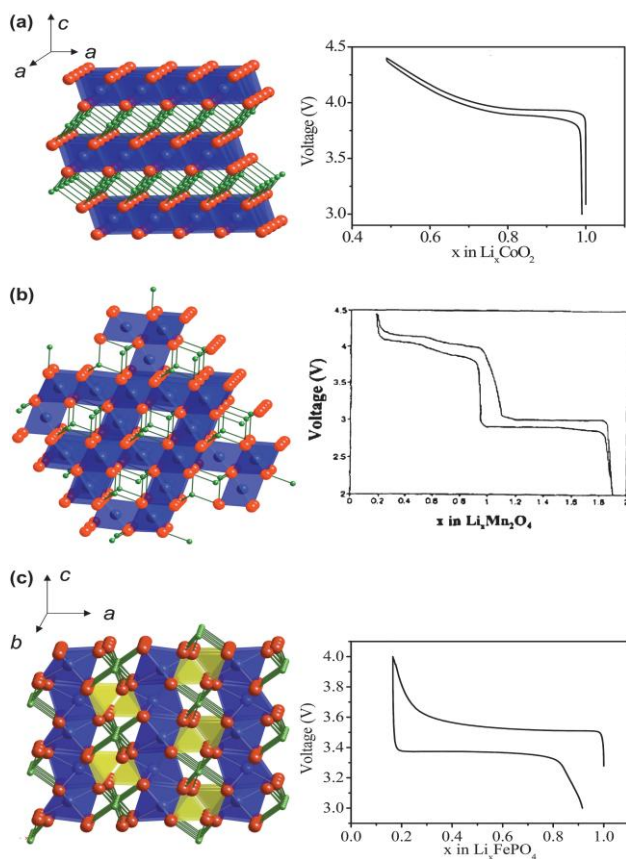


Fig. 2.2 Crystalline structures and voltage–composition curves of (a) layered- LiCoO_2 (R3-m S.G.)—oxygen (red) layers are stacked in ABC sequence, with lithium (green) and cobalt (blue) residing in the octahedral sites of the alternating layers; (b) spinel- LiMn_2O_4 (Fd-3m S.G.)—lithium (green) resides in the tetrahedral sites formed by oxygen stacking; and (c) olivine- LiFePO_4 (Pnma S.G.)—phosphor (yellow) and oxygen form tetrahedral units linking planes of corner-sharing FeO_6 octahedra. Adapted from Ref [39] (Y. S. Meng, and M. E. A.-de Dompablo, *Energy Environ. Sci.*, 2009, **2**, 589)

2.2.2 Anode

Anode materials have three typical reaction mechanisms and they are shown in Fig. 2.3 [47]. An ideal anode material should have the potential adjacent with the standard electrode potential of Li metal. Furthermore, anode materials preferred to have the high volumetric and gravimetric energy density, good cycleability, high columbic efficiency, high rate characteristics, and safety.

Carbon is the most typical intercalation material that used in majority of anode materials according to its negative redox potential, (0.1 – 0.2 V vs. Li/Li⁺), and dimensional stability resulting in good cycle performance. The insertion of lithium ion into carbon matrix proceeds due to the equation shown before.



The amount of x is varied by depending on the structure of the carbon, such as crystallinity, microstructure and the micromorphology. Carbon can be divided into graphitic and non-graphitic by their structural characteristics. The former one has graphene layers with or without structural defects, including natural graphite, artificial graphite, and pyrolytic graphite. Non-graphitic carbons are often called by disordered carbon. But they have structural without long-range crystallographic order in c-direction and consist of crystalline

and amorphous phase. Additionally, non-graphitic carbons are generally prepared by the pyrolysis of organic polymer or hydrocarbon precursor at temperature below ~ 1500 °C.

Graphite can uptake Li ion per six carbon atoms at room temperature, which amount to specific capacity of 372 mA h g^{-1} [48]. A general feature of intercalation into graphite can be characterized by “staging phenomena”, so under potentiodynamic control, several voltage plateaus which are according to the consecutive two-phase reactions related to the Li-carbon binary phases can be observed [49, 50].

Materials that undergo alloying reaction with lithium as anode include Sn, Sb, Si, Ge, Al, and Ga. These metals alloy with lithium over 0 V Li/Li⁺ at room temperature and show much higher specific capacity when compared with graphite. Specific capacities and capacity densities for selected alloying reactions are shown in Fig.2.4 [47]. However, the major limitation when using as LIBs anode is the severe volume change during charge/discharge, leading to cracks on the active material, electrical disconnection, and finally capacity fading. Many methods such as morphology control and nanocomposites with carbon have been introduced to overcome these limitations [51].

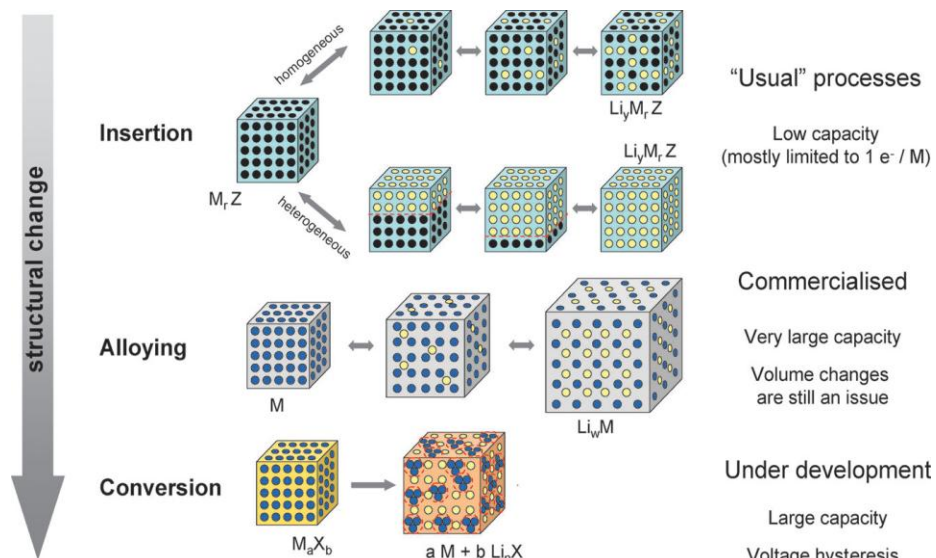


Fig. 2.3 A schematic representation of the different reaction mechanisms observed in electrode materials for lithium batteries. Black circles: voids in the crystal structure, blue circles: metal, yellow circles: lithium. Adapted from Ref [47] (M. R. Palacin, *Chem. Soc. Rev.*, 2009, **38**, 2565)

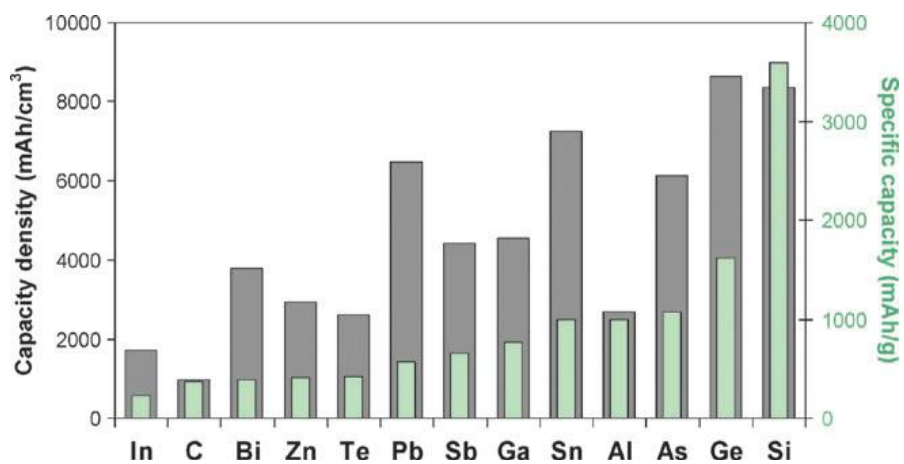


Fig. 2.4 Specific capacities and capacity densities for selected alloying reactions. Values for graphite are given as a reference. Adapted from Ref [47] (M. R. Palacin, *Chem. Soc. Rev.*, 2009, **38**, 2565)

Another kind of material that can obtain higher specific capacity than carbon-based materials is transition metal oxides and they are undergoing conversion reaction. Conversion reactions are lithium reactions with binary M-X compounds (M=transition metal and X=O, N, F, S, P) in which M-X compound is reduced to nanoscale metal clusters (2-5 nm) dispersed in a Li_nX matrix as follow equation.



n is formal oxidation state of X.

Materials based on conversion reaction have much higher theoretical capacity than that of graphite (Fig. 2.5) [52]. Furthermore, the operation potential can be tuned by using different metal cations because the strength of M-X bond is associated with equilibrium voltage. However, they exhibit a complete structural change and a large hysteresis in charge/discharge voltage, which is connected with high energetic barrier in breakage of M-O bond.

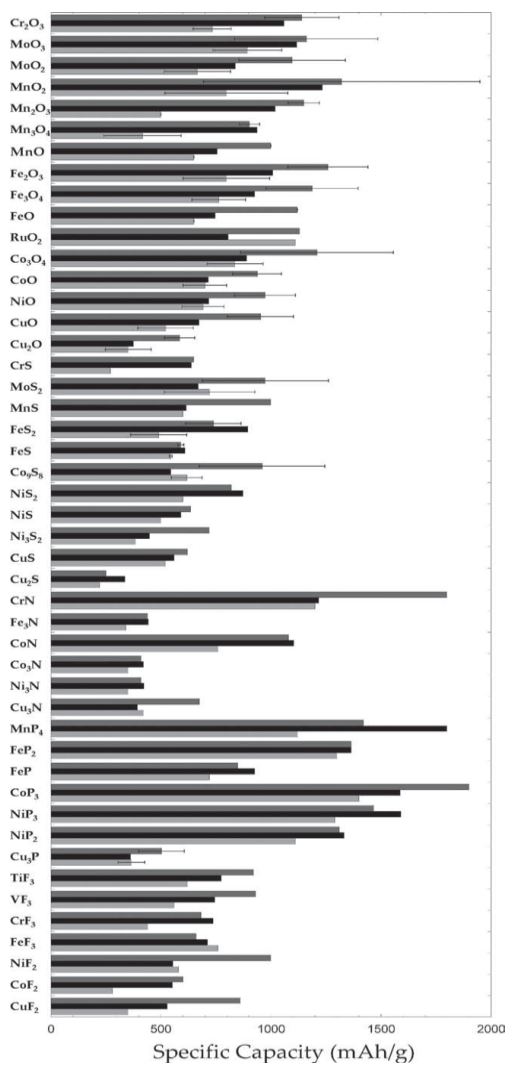


Fig. 2.5 Theoretical (black bars), first discharge (dark grey), and charge (light grey) specific gravimetric capacities of different compounds that react with lithium through a conversion reaction. Adapted from Ref [52] (J. Cabana, L. Monconduit, D. Larcher, and M. R. Palacín, *Adv. Mater.*, 2010, **22**, E170)

2.2.3 Electrolyte

The electrolyte is composed of solvent and salt that plays an important role as a medium for ion transfer between cathode and anode. In a battery system, electrolyte the electrochemical stability of the electrolyte is closely connected with kinetic parameter rather than thermodynamic term. This is directly related to the cycleability, safety, and rate characteristics. However, it is challenged by the oxidizing and reducing nature of the cathode and anode. In order to become an ideal electrolyte, it should meet the following properties; (1) it should be a good ionic conductor and electronic insulator. (2) It should have a wide electrochemical window in case decomposing within the range of the working potentials of cathode and anode. (3) It should be inert to other cell components such as separators, current collectors for electrode, and cell packaging materials. (4) It should be stable to other various abuses, such as electrical, mechanical, or thermal ones. (5) The components of electrolytes should be eco-friendly.

Nowadays, commercial lithium ion batteries are generally using carbonate-based electrolyte. It is composed of two different structures, cyclic carbonate and linear carbonate. Cyclic carbonate has the high dielectric constant and linear carbonate shows low viscosity and high conductivity. By dissolving 1.0 M of LiPF_6 into these two kinds of

carbonate, this can be used in commercial battery system. But these are toxic and flammable. Thus, ionic liquid is actively researched according to its low volatility and flame resistivity.

Chapter 3. Experimental

3.1 Preparation of material

Graphene oxide (GO) was prepared from graphite powder (Aldrich, < 20 micron) according to an improved Hummer's method [53]. Briefly, 3 g of graphite and a 9:1 mixture of concentrated $\text{H}_2\text{SO}_4/\text{H}_3\text{PO}_4$ (90 : 10 ml) were stirred together in an ice bath for 1 hour. Then, 18 g of KMnO_4 were slowly added and reacted for 1 hour. After the mixture was stirred for 12 hours at 50 °C, 350 ml of DI water were added. 5 ml of H_2O_2 (30 wt%) were slowly added and the solution was washed with 1 : 10 HCl aqueous solution followed by repeated washings with DI water. Finally, the brown powder was dried at 60 °C overnight.

For comparison, we have synthesized bare graphene (G) without adding the hydrazine solution. Other conditions were the same as those for the synthesis of NG.

For the Mn_3O_4 /nitrogen-doped graphene composites (M-NG) synthesis, 0.2 g of GO and 1g of manganese (II) acetate were added to 65 ml of DI water followed by sonication for 1 hour. Then, 500 L of hydrazine monohydrate (80 wt%) were slowly added. After 30 min of stirring, the mixture was transferred to 100 ml of Teflon-lined stainless

steel autoclave for hydrothermal reaction at 180 °C for 12 hours. After cooling down to room temperature, a black product was isolated by filtration and dried at 90 °C overnight.

Sample of Mn₃O₄/graphene composites (M-G) was prepared for comparison. The experimental steps for this sample were the same as for the synthesis of M-NG, but with the replacement of hydrazine hydrate by NaOH for Mn₃O₄/graphene (NaOH can act as a mineralizer).

Nitrogen-doped graphene (NG) was prepared by hydrazine reduction of GO. GO was dispersed in 50 ml of DI water (2 mg ml⁻¹) and this solution was transferred to 100 ml of Teflon-lined autoclave. Then, it was heated at 180 °C for 12 hours. The product was filtered and then dried.

3.2 Preparation of composite electrode

For the preparation of the working electrode, first of all, active material, super P(as a conductive agent) and polyvinylidene fluoride(as a binder) were stored in a convection oven at 100 °C for longer than 1 hour to eliminate moisture. Then a slurry composed of active material, super P and polyvinylidene fluoride (70: 15: 15 in weight ratio) in n-methyl-2-pyrrolidone was uniformly plastered on a Cu foil and dried

in a vacuum oven at 50 °C for 1 hour. After drying, the electrode was roll-pressed and dried again in a vacuum oven at 120 °C overnight.

3.3 Preparation of half cell

2016 type coin cell were assembled with a Cu foil electrode (22 µm thick, 11 mm in diameter), a polypropylene separator, lithium metal foil as a counter electrode and a reference electrode, and the electrolyte was 1.0 M LiPF₆ dissolved in ethylene carbonate (EC) and diethyl carbonate (DEC) (1:1 in volume ratio). All processes were performed in an argon-filled glove box.

3.4 Characterization

X-Ray diffraction (XRD) patterns were obtained on a Bruker D-5005 with Cu K α radiation ($\lambda = 1.5406 \text{ \AA}$) at 40 kV and 40 mA with a scan range of 10°~90°. The morphologies of samples were characterized by carrying out field emission scanning electron microscopy (FE-SEM, Hitachi S-4800). A JEM-2010 transmission electron microscope (TEM) equipped with a field emission gun and operated at 200 kV was used for high-resolution TEM measurements. For thermogravimetric analysis (TGA) measurements, a METTLER TOLEDO TGA/DSC 1 thermogravimetry analyzer was used with a

heating rate of $10\text{ }^{\circ}\text{Cmin}^{-1}$ in air. X-ray photoelectron spectroscopy (XPS) experiments were performed by AXIS-His spectrometer (KRATOS) with a monochromatic Al $K\alpha$ source (1486.6 eV) with at 12 kV and 10 mA current. The binding energies were shifted for charging using C1s to 284.5 eV. Flash 1112 (CE Instrument, Italy) Element 70 Analyzer was used to confirm the element contents in samples.

3.5 Electrochemical measurement

The voltage window was between 0.01 and 3.0 V vs. Li/Li^+ . The cells were galvanostatically charged and discharged with a WBCS3000 cycler (WonA Tech, Korea) at room temperature. The loading level is about 2 mg cm^{-2} . In term of capacity of the M-NG, it is based on the total weight of composite. Cyclic voltammetry (CV) was also conducted with a WBCS3000 cycler and the scan rate was 0.1 mV s^{-1} . Electrochemical impedance spectroscopy measurements were carried out in the range of the frequency from 100 kHz to 50 mHz with an AC signal amplitude of 5 mV.

Chapter 4. Results and discussion

4.1 The analysis of powder

The typical structure and morphology of M-NG were studied by FE-SEM and TEM. As shown in Figs. 1a and 1b, M-NG has a wrinkled structure, consisting of many sheets, which is the same as the general structure of conventional graphene sheets. All the Mn_3O_4 nanoparticles were found on the surface of graphene. These images showed that small Mn_3O_4 nanoparticles were embedded between thin graphene layers. The TEM images (Figs. 4.1c and 4.1d) showed that the Mn_3O_4 nanoparticles were uniformly distributed in the form of small particle clusters on the surface of the graphene sheets. In contrast, these similar structures can also be observed in M-G composite (Figs. 4.2a and 4.2b). In contrast, bare Mn_3O_4 nanoparticles prepared without the graphene sheets were severely aggregated (Figs 4.3a and 4.3b). It is known that the interaction between the oxygen-containing functional groups on the surface of graphene sheets and metal ions prevents the agglomeration and growth of metal oxide nanoparticles to some extent [54]. According to previous reports, these unique structures provide more active sites for lithium ions and allow for effective ion and electron transport during cycling, leading

to excellent electrochemical performance [55, 56].

The HR-TEM image of M-NG is presented in Fig. 4.1d. The composite was formed by stacked graphene sheets with highly crystalline Mn_3O_4 nanoparticles. The inset clearly shows the stack of graphene sheets (*cf.* black colored arrow), which consists of less than 15 layers. The Mn_3O_4 nanoparticles have crystal lattice fringes of 0.49 nm, corresponding to the (101) plane. Thus, the Mn_3O_4 nanoparticles prepared by our method not only had high crystallinity but also were embedded in the interlayers between the graphene nanosheets. These unique properties provide the composite with superior stability and facilitate fast lithium ion transfer during the lithiation-delithiation process.

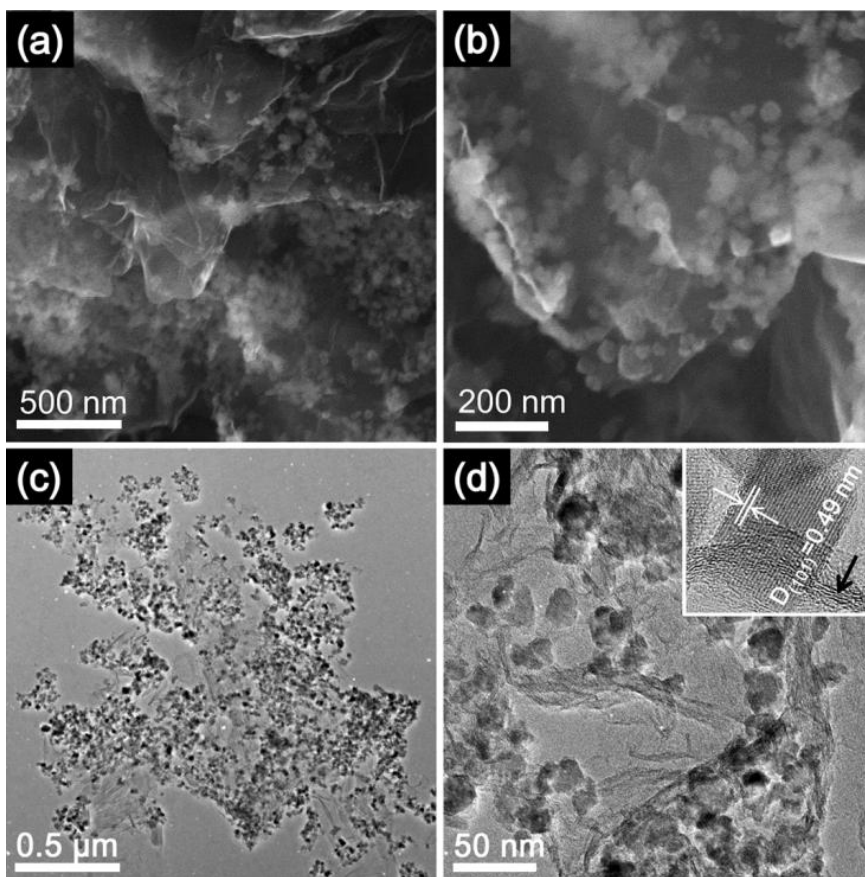


Fig. 4.1 (a, b) SEM images and (c, d) TEM images of M-NG composite (inset: HR-TEM image of Mn_3O_4 nanoparticle on the graphene sheet).

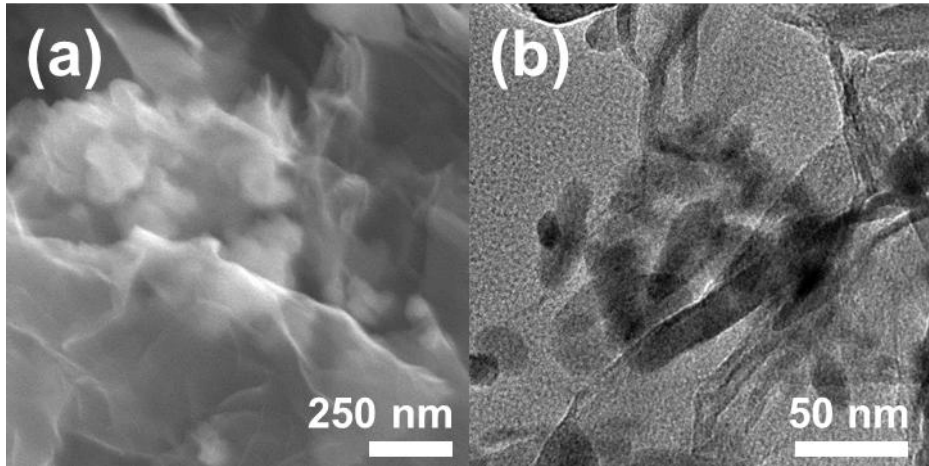


Fig. 4.2. SEM images of M-G composite.

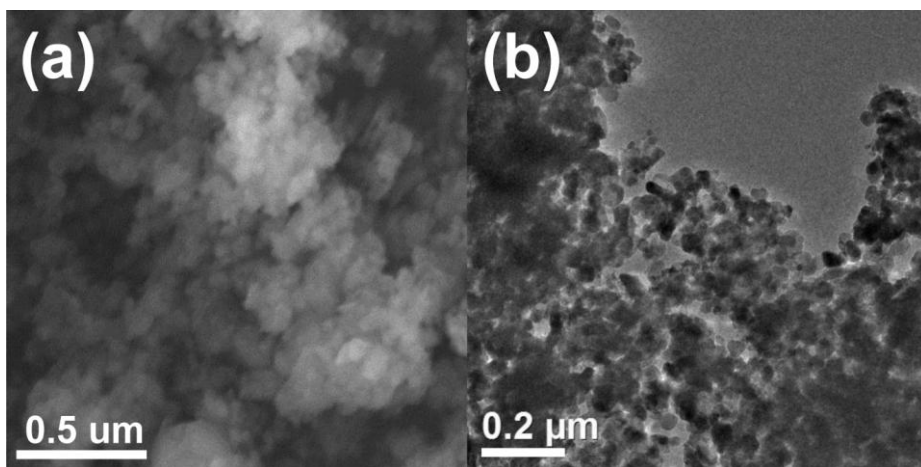


Fig. 4.3. SEM and TEM images of bare Mn_3O_4 nanoparticles.

Fig. 4.4a shows the X-ray diffraction (XRD) patterns of the GO, NG, and M-NG composites. After the hydrothermal reaction, the diffraction peak at 10° for GO shifted to a higher angle (*ca.* 25°), indicating the reduction of GO [57]. Further, the XRD spectrum of graphene had broad peaks, which are typical to an amorphous carbon structure, showing that the stacking of graphene layers was disordered [58]. The XRD patterns of the M-NG composite clearly indicated strong crystallization of the tetragonal spinel Mn_3O_4 phase (JCPDS card no. 24-0734), as well as a broadened peak at *ca.* 25° , corresponding to the graphene (002) plane diffraction. No impurities were found in the XRD patterns, confirming the high purity of the samples. The average crystallite size was *ca.* 48 nm, as calculated from Scherrer's equation. These results were in good agreement with the previous HR-TEM data.

To accurately determine the graphene content in M-NG, TGA was carried out in air, from 25 to 800 $^\circ\text{C}$ (Fig. 4.4b). In the temperature range 25 to 100 $^\circ\text{C}$, there was a small degree of weight loss, attributed to the loss of water. When the temperature increased to 330 $^\circ\text{C}$, graphene started to decompose and completely disappeared at about 600 $^\circ\text{C}$. Based on this result, the weight of graphene in M-NG was determined to be about 36 %.

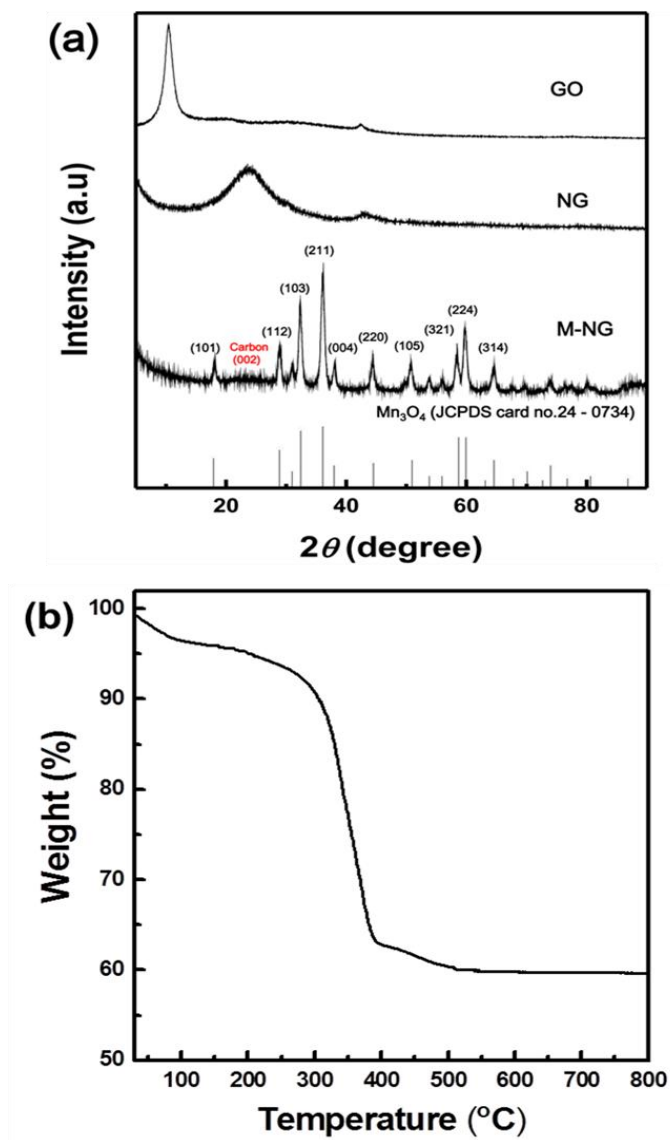


Fig. 4.4 (a) XRD patterns of GO, NG and M-NG composite, (b) TGA curve of M-NG composite.

To characterize the M-NG in detail, Raman spectroscopy and X-ray photoelectron spectroscopy (XPS) were performed to determine the electronic structure and compositions. Raman spectra of GO, NG, bare Mn_3O_4 , and the M-NG composite are shown in Fig. 4.5. In all cases except for the bare Mn_3O_4 , broad peaks were observed at 1340 and 1600 cm^{-1} , which were assigned to the graphene D and G bands, respectively. According to previous reports, the D peak is related to edges or disordered layers, and the G peak corresponds to the E_{2g} mode of sp^2 carbon atoms [60, 61]. Therefore, the intensity ratio of the D and G bands (I_D/I_G) provides information about the disorder and crystallite size of the graphitic layers. The intensity ratios, I_D/I_G , for NG and M-NG were (1.07) and (1.04), respectively, and both were higher than that of GO (0.89), indicating that the reduction of GO leads to more disordered layers as well as a decrease in the number of graphene layers [61]. Furthermore, the M-NG composite peaks at 323 cm^{-1} , 378 cm^{-1} (very weak), and 645 cm^{-1} (dominant) were attributed to crystalline Mn_3O_4 , as observed for the bare Mn_3O_4 . These results confirmed that the M-NG composite is composed of pure graphene sheets and crystalline Mn_3O_4 nanoparticles.

Figs. 4.6a and 4.6b show the deconvoluted C 1s spectra of GO and M-NG, respectively. In the case of GO, the peaks at 284.5, 286.4,

288.0, and 289.0 eV were attributed to the C-C (sp^2 carbon in the graphene basal plane), C-O, C=O, and O-C=O groups, respectively. After the hydrothermal reaction, the C/O ratio rapidly decreased in M-NG, indicating that GO was almost reduced by hydrazine hydrate. Furthermore, in the spectrum of M-NG, a new component appeared at 285.2 eV, which could be attributed to the C-N bonds. These results revealed that hydrazine hydrate can act both as a reducing agent and as a nitrogen source. The manganese oxidation state was identified from the multiplet splitting of the Mn 2p peak. The splitting width of the two peaks at 654.7 and 642.9 eV was 11.8 eV, which is in accordance with the value in an earlier report on Mn_3O_4 [60]. The N 1s peak of M-NG consisted of two Lorentzian peaks, as shown in Fig. 4.5d. Pyrrolic N (400.1 eV) was more dominant than pyridinic N (398.3 eV), and these accounted for 78.8 % and 21.2 % in the N binding configuration, respectively. These nitrogen doping should inherit from the hydrazine hydrate. However, the mechanism of nitrogen doping using hydrazine is still unclear [62].

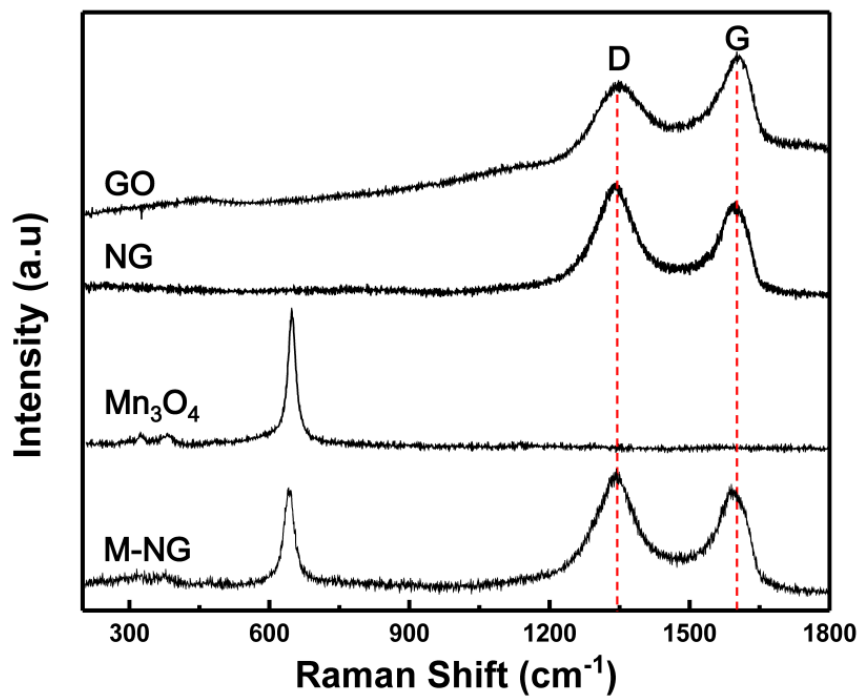


Fig. 4.5 Raman spectra of GO, NG, bare Mn₃O₄ and M-NG composite.

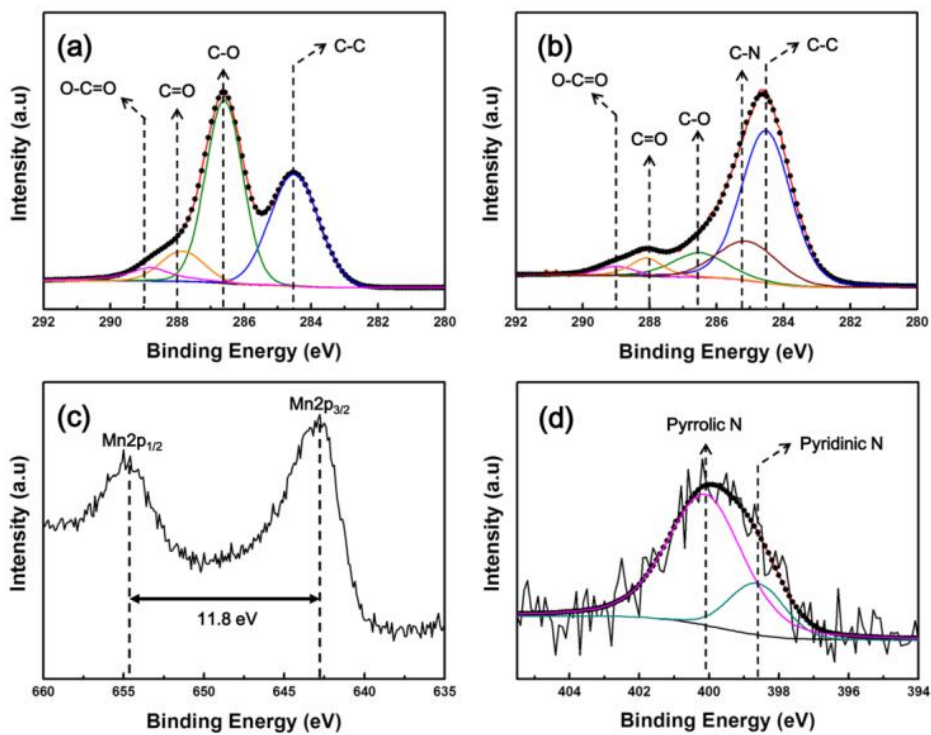


Fig. 4.6 XPS spectra of the (a) C 1s region of GO, (b) C 1s region, (c) Mn 2p region, and (d) N 1s region of M-NG composite.

According to previous reports, the coexistence of electron deficiency and vacancies at the pyridine-like defects offers a feasible pathway for lithium ion penetration of the graphene layers [34, 63]. Therefore, nitrogen doping results in enhanced electrochemical performance. The nitrogen content in M-NG was confirmed by elemental analyzer, and 2 wt% of the sample was shown to be composed of nitrogen (Table 1).

Table 1 Composition (wt%) of the GO, NG, M-NG and Mn₃O₄ resulted from elemental analyzer

Sample	C	H	N
GO	41.2	3.2	0
NG	78.8	1.6	5.4
M-NG	30.9	0.8	2
Mn ₃ O ₄	0.56	0.41	0

4.2 The electrochemical analysis

To evaluate the performance of lithium batteries with the M-NG electrode, the cells were galvanostatically charged and discharged between 3.0 V and 0.01 V. In this voltage range, the mechanism underlying the reaction between lithium and Mn_3O_4 can be described by the following electrochemical conversion:[14, 64, 65]



At a current density of 200 mA g^{-1} (Fig. 4.7a), the first discharge capacity of M-NG was 1275 mA h g^{-1} . In the first discharge curve, it was observed that reduction reactions mainly occurred at 0.25 V. The capacity delivered between 2.0 and 0.25 V was around 380 mA h g^{-1} , which was related to two reactions: [64-66] (1) the reaction between lithium ions and the reduced graphene oxide layer and (2) the decomposition of the electrolyte and the formation of a solid electrolyte interphase (SEI) layer. The large plateau at ca. 0.25 V corresponded to the reduction reaction between lithium and manganese oxide to form lithium oxide and metallic Mn. In the subsequent cycles, the main plateaus were observed at a higher voltage (~0.4 V), indicating that nanoscale particles after the first

discharge resulted in a low overpotential [65]. In the charging curves, the capacity above 2.0 V was related to the de-insertion of lithium ions in the reduced graphene oxide layer. In the voltage profiles of M-G composites, the first discharge capacity was 1397 mA h g^{-1} , which is higher than that of M-NG. However, the first reversible specific capacity of M-G was lower, indicating that the capacity retention property of M-NG is better than that of M-G. There were no significant differences of the profile shape between M-NG and M-G. The bare Mn_3O_4 delivered a capacity about 1250 mA h g^{-1} at the first cycle. The shape of the profiles was similar to that in the case of M-NG, except that the capacity above 2.0 V during the charge process in Mn_3O_4 was much lower than that in M-NG.

Cyclic voltammetry (CV) was carried out at a scanning rate of 0.1 mV s^{-1} in the voltage range of 3.0 V to 0.01 V to acquire additional information (Fig. 4.7d). In the first cycle, the small cathodic peaks observed at ca. 0.71 V for M-NG composite, which were related to the decomposition of electrolyte and formation of the solid electrolyte interphase (SEI) layer. The spiky reduction peaks below 0.2 V in M-NG composite are assigned to reduction reaction of lithium ion with manganese oxide. In addition, the peak in M-NG composite is also related to reduction reaction of lithium ion with

graphene. The strong peaks about 1.25 are observed in the samples in the anodic process, which is attributed to oxidation of metallic manganese to manganese ions. The oxidation peak above 2.0 V in M-NG composite is due to de-insertion of lithium ions in the reduced graphene layers.

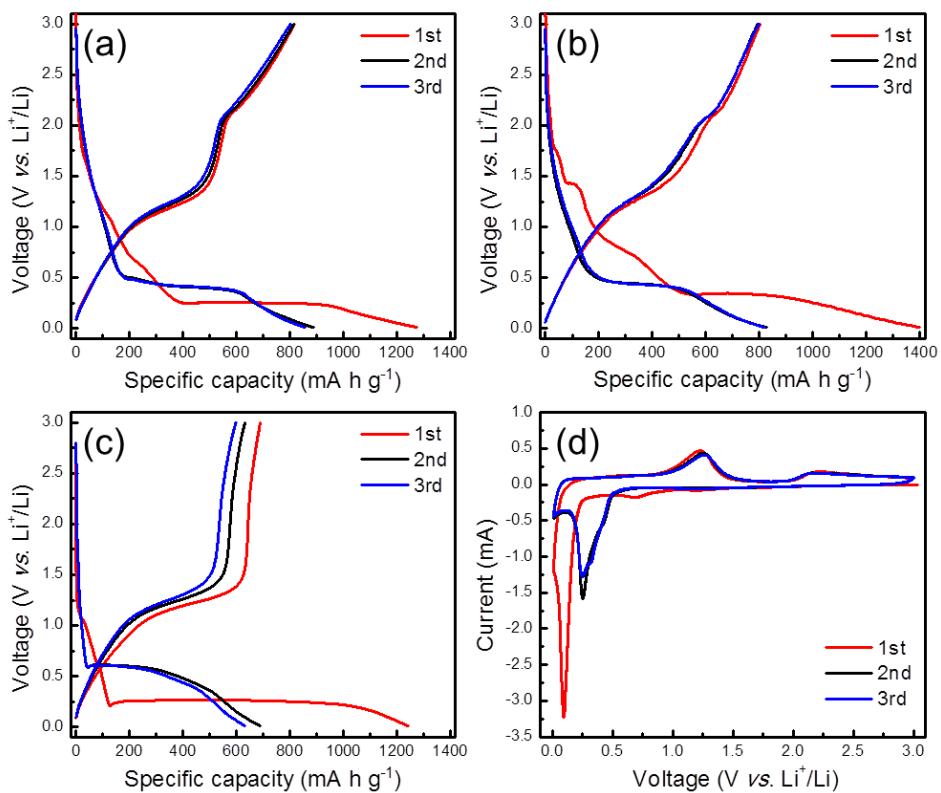


Fig. 4.7 Voltage profiles of (a) M-NG composite and (b) M-G composite and (c) bare Mn_3O_4 and (d) Cyclic voltammograms of M-NG composite at a scanning rate of 0.1 mV s^{-1}

The cycle performances of M-NG, M-G and Mn_3O_4 in the voltage range 0.01–3.0 V and at a current density of 200 mA g^{-1} are shown in Fig. 4.8a. These results showed the influence of nitrogen-doping on the capacity retention properties. At the initial cycle, the capacity of M-G was higher value of 1397 mA h g^{-1} than that of M-NG. However, it continuously decreased to 703 mA h g^{-1} after 40 cycles. In contrast, the M-NG still maintained its specific capacity of 800 mA h g^{-1} , which is more stable and higher performance than that of M-G. The enhanced cycling performance of M-NG compared with M-G can be caused by the nitrogen doping, which gives rise to a stronger synergistic effect between the nitrogen-doped graphene and the Mn_3O_4 particles than the undoped-graphene. These results are consistent with those of previous studies [63, 67]. Also the bare Mn_3O_4 nanoparticles delivered a capacity about 1250 mA h g^{-1} at the first discharge, it gradually decayed during the cycling. In rate properties, three different electrodes showed a similar tendency.

The rate capabilities of M-NG, M-G and Mn_3O_4 are shown in Fig. 4.8b. The M-NG showed the highest value in all different current density, demonstrating the high power capability of M-NG. It is clear that the reversible capacities of M-NG and M-G were still maintained higher than that of bare Mn_3O_4 particles even at very high current

density (at the 2 A g⁻¹, 382, 323 and 233 mA h g⁻¹ for M-NG, M-G, Mn₃O₄, respectively). This phenomenon can be attributed to the excellent electrical and mechanical properties of graphene, which provides high electron transfer and inhibits the aggregation of Mn₃O₄ particles. On the other hand, the difference of reversible capacity between M-NG and M-G is due to the nitrogen-doping on graphene.

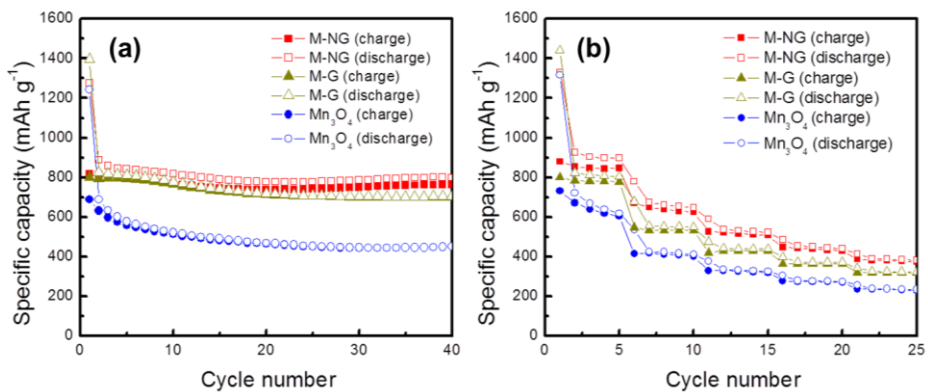


Fig. 4.8 (a) Cycle performances of M-NG composite (squares, red), M-G composite (triangle, dark yellow) and bare Mn₃O₄ (circles, blue) at a current density of 200 mA g⁻¹ (b) Rate properties of M-NG composite (squares, red), M-G composite (triangle, dark yellow) and bare Mn₃O₄ (circles, blue).

To confirm the nitrogen doping effects on the graphene, G and NG were evaluated at a current density of 200 mA g^{-1} . As shown in Fig. 4.9, the NG displayed elevated capacity and excellent cycling stability, compared to G. Despite the almost same first discharge capacity of two different electrodes, the reversible capacity of NG was 471 mA h g^{-1} after 40 cycles, while that of G was just 353 mA h g^{-1} . These results exhibited that the nitrogen doping can improve the electrochemical properties as already reported [68, 69].

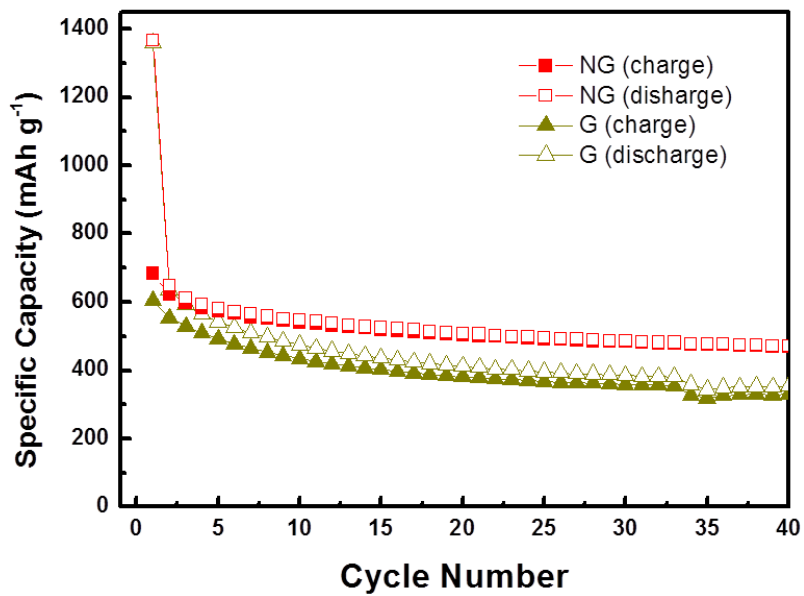


Fig. 4.9 Cycle performances of G and NG cycled at 200 mA g⁻¹ for 40 cycles.

The electrochemical impedance spectroscopy measurements (EIS) of M-NG composite and bare Mn_3O_4 at charged state after 1 cycle were performed to further understand the improved electrochemical properties of M-NG composite in Fig. 4.10. The semicircle in the high and middle frequency ranges are related to SEI resistance and charge transfer resistance, respectively. This indicates that both SEI resistance and charge transfer resistance of M-NG composite are much smaller than those of bare Mn_3O_4 . This result is consistent with previous cycle and rate properties.

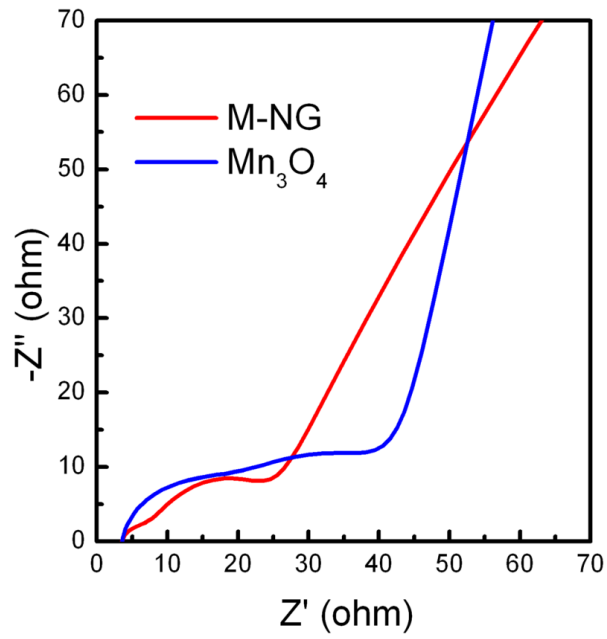


Fig. 4.10 Nyquist plots of the M-NG composite and bare Mn_3O_4 at the charged state after 1 cycle.

The enhanced electrochemical performance of M-NG, including the high capacity, excellent cyclic stability, and good rate capability, could be attributed to the following three advantages. First, the graphene layers can provide a void space that offsets the volume expansion of Mn_3O_4 nanoparticles, thus preventing their aggregation during cycling. On the other hand, pure Mn_3O_4 nanoparticles exhibit less capacity and cycling performance due to the large volume change during the cycling, resulting in the aggregation of active materials. This fact was confirmed by TEM (Fig. 4.11). Second, because of its intrinsic excellent electric properties, the graphene layers provide a high electric pathway to each Mn_3O_4 nanoparticle, which can improve the rate property. Third, nitrogen doping of graphene not only increases its conductivity but also provides a greater number of active sites by raising the Fermi level toward the conduction band, leading to excellent electrochemical performance.

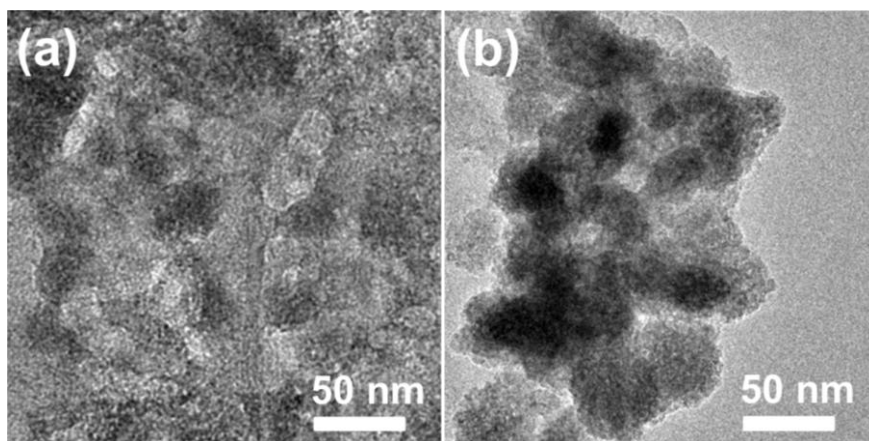


Fig. 4.11 HR TEM images of (a) M-NG and (b) bare Mn_3O_4 nanoparticles after 30 cycles at 200 mA g^{-1} .

Chapter 5. Conclusions

In summary, we have developed a facile hydrothermal route to grow small Mn_3O_4 nanoparticles on the surface of N-doped graphene using hydrazine hydrate both as a reducing agent and as a nitrogen source. The synthesized Mn_3O_4 nanoparticles in the composite, directly grown on the 3D structured surface of the graphene sheet, can be smaller than the Mn_3O_4 nanoparticles synthesized without the graphene sheet, because of the interaction between the functional groups of graphene oxide and the positively charged manganese ions. When used as an anode material in LIBs, the synthesized composite with high nitrogen content exhibits high specific capacity, excellent cycling stability, and rate capability because graphene can act as an electron conductor and a physical buffer limiting the volume expansion of the manganese oxide nanoparticles upon polarization.

In addition, nitrogen doping can allow for fast electron and ion transfer by decreasing the energy barrier, thus leading to high electrochemical performance. Therefore, our strategy can be considered as a promising means of synthesizing N-doped graphene composites with embedded metal oxide nanoparticles for use as efficient anode materials in LIBs.

References

- [1] M. Winter, R.J. Brodd, *Chem. Rev.*, 2004, **104**, 4245.
- [2] M. S. Whittingham, *Chem. Rev.*, 2004, **104**, 4271.
- [3] M. S. Whittingham, *Science*, 1979, **192**, 1126.
- [4] C. M. Hayner, X. Zhao and H. H. Kung, *Annu. Rev. Chem. Biomol. Eng.*, 2012, **3**, 445.
- [5] M.M. Thackeray, C. Wolverton and E. D. Isaacs, *Energy Environ. Sci.*, 2012, **5**, 7854.
- [6] L. Lu, X. Han, J. Li, J. Hua and M. Ouyang, *J. Power Sources*, 2013, **226**, 272.
- [7] S.-K. Park, S.-H. Yu, S. Woo, B. Quan, D.C. Lee, M.K. Kim, Y.-E. Sung and Y. Piao, *Dalton Trans.*, 2013, **42**, 2399.
- [8] S.-K. Park, S.-H. Yu, S. Woo, J. Ha, J. Shin, Y.-E. Sung and Y. Piao, *Crystengcomm.*, 2012, **14**, 8323.
- [9] S. Baek, S.-H. Yu, S.-K. Park, A. Pucci, C. Marichy, D.C. Lee, Y.-E. Sung, Y. Piao and N. Pinna, *RSC Adv.*, 2012, **2**, 13038.
- [10] C. Lei, F. Han, D. Li, W.C. Li, Q. Sun, X.Q. Zhang and A.H. Lu, *Nanoscale*, 2013, **5**, 1168.
- [11] H.S. Kim, Y. Piao, S.H. Kang, T. Hyeon and Y.-E. Sung,

- Electrochem. Commun.*, 2010, **12** 382.
- [12] X. Xiao, X. Liu, H. Zhao, D. Chen, F. Liu, J. Xiang, Z. Hu and Y. Li, *Adv. Mater.*, 2012, **24**, 5762.
- [13] Z.C. Bai, N. Fan, C.H. Sun, Z.C. Ju, C.L. Guo, J. Yang, Y.T. Qian, *Nanoscale*, 2013, **5**, 2442.
- [14] H.L. Wang, L.F. Cui, Y.A. Yang, H.S. Casalongue, J.T. Robinson, Y.Y. Liang, Y. Cui and H.J. Dai, *J. Am. Chem. Soc.*, 2010, **132**, 13978.
- [15] J.Y. Qu, F. Gao, Q. Zhou, Z.Y. Wang, H. Hu, B.B. Li, W.B. Wan, X.Z. Wang and J.S. Qiu, *Nanoscale*, 2013, **5**, 2999.
- [16] L.W. Ji and X.W. Zhang, *Electrochem. Commun.*, 2009, **11**, 795.
- [17] H. Cheng and K. Scott, *J. Power Sources*, 2010, **195**, 1370.
- [18] A.L.M. Reddy, M.M. Shaijumon, S.R. Gowda and P.M. Ajayan, *Nano Lett.*, 2009, **9**, 1002.
- [19] A.K. Geim and K.S. Novoselov, *Nat. Mater.*, 2007, **6**, 183.
- [20] K.S. Novoselov, A.K. Geim, S.V. Morozov, D. Jiang, M.I. Katsnelson, I.V. Grigorieva, S.V. Dubonos and A.A. Firsov, *Nature*, 2005, **438**, 197.
- [21] B. Jang, E. Choi and Y. Piao, *Mater. Res. Bull.*, 2013, **48**, 834.
- [22] M.H. Liang and L.J. Zhi, *J. Mater. Chem.*, 2009, **19**, 5871.
- [23] S.-K. Park, S.-H. Yu, N. Pinna, S. Woo, B. Jang, Y.H. Chung, Y.H.

- Cho, Y.-E. Sung and Y. Piao, *J. Mater. Chem.*, 2012, **22**, 2520.
- [24] B. Jang, M. Park, O.B. Chae, S. Park, Y. Kim, S.M. Oh, Y. Piao and T. Hyeon, *J. Am. Chem. Soc.*, 2012, **134**, 15010.
- [25] J. Ye, J. Zhang, F.X. Wang, Q.M. Su and G.H. Du, *Electrochim. Acta*, 2013, **113**, 212.
- [26] Z.X. Song, Y.J. Zhang, W. Liu, S. Zhang, G.C. Liu, H.Y. Chen and J.S. Qiu, *Electrochim. Acta*, 2013, **112**, 120.
- [27] C.-T. Hsieh, C.-Y. Lin, Y.-F. Chen and J.-S. Lin, *Electrochim. Acta*, 2013, 111, 359.
- [28] L. Li, K.H. Seng, H.K. Liu, I P. Nevirkovets and Z.P. Guo, *Electrochim. Acta*, 2013, **87**, 801.
- [29] Y.J. Mai, X.L. Wang, J.Y. Xiang, Y.Q. Qiao, D. Zhang, C.D. Gu and J.P. Tu, *Electrochim. Acta*, 2011, **56**, 2306.
- [30] L. Li, Z.P. Guo, A.J. Du and H.K. Liu, *J. Mater. Chem.*, 2012, **22**, 3600.
- [31] I. Nam, N.D. Kim, G.-P. Kim, J. Park and J. Yi, *J. Power Sources*, 2013, **244**, 56.
- [32] B. Jang, O.B. Chae, S.-K. Park, J. Ha, S.M. Oh, H.B. Na and Y. Piao, *J. Mater. Chem. A*, 1 2013, **1**, 15442.
- [33] H.B. Wang, C.J. Zhang, Z.H. Liu, L. Wang, P.X. Han, H.X. Xu, K.J. Zhang, S.M. Dong, J.H. Yao and G.L. Cui, *J. Mater. Chem.*,

- 2011, **21**, 5430.
- [34] C.C. Ma, X.H. Shao and D.P. Cao, *J. Mater. Chem.*, 2012, **22**, 8911.
- [35] Z.H. Wen, X.C. Wang, S. Mao, Z. Bo, H. Kim, S.M. Cui, G.H. Lu, X.L. Feng and J.H. Chen, *Adv. Mater.*, 2012, **24**, 5610.
- [36] K.J. Zhang, P.X. Han, L. Gu, L.X. Zhang, Z.H. Liu, Q.S. Kong, C.J. Zhang, S.M. Dong, Z.Y. Zhang, J.H. Yao, H.X. Xu, G.L. Cui and L.Q. Chen, *ACS Appl. Mater. Interfaces*, 2012, **4**, 658.
- [37] X. Wang, X. Cao, L. Bourgeois, H. Guan, S. Chen, Y. Zhong, D.-M. Tang, H. Li, T. Zhai, Li, Y. Bando, D. Golberg, *Adv. Funct. Mater.*, 2012, **22**, 2682.
- [38] R. Liu, J. Duay and S. B. Lee, *Chem. Commun.*, 2011, **47**, 1384
- [39] Y. S. Meng and M. E. A.-de Dompablo, *Energy Environ. Sci.*, 2009, **2**, 589
- [40] J.N. Reimers and J.R. Dahn, *J. Electrochem. Soc.*, 1992, **139**, 2091.
- [41] J.N. Reimers, J.R. Dahn and U. von Sacken, *J. Electrochem. Soc.*, 1993, **140**, 2752.
- [42] J. Baker, R. Koksang and M. Y. Saidi, *Solid State Ionics*, 1996, **89**, 25.
- [43] L. G. Cemourgues, C. Denage and C. Delmas, *J. Power Sources*,

- 1994, **52**, 269.
- [44] M. Yoshio, Y. Todorov, K. Yamato, H. Noguchi, J. Itoh, M. Okada and T. Mouri, *J. power Sources*, 1998, **74**, 46.
- [45] M. Thackeray, W. David, P. Bruce and J. Goodenough, *Mater. Res. Bull.*, 1983, **198**, 461.
- [46] A. Pahdi, K. Nanjundaswamy and J. Goodenough, *J. Electrochem. Soc.*, 1997, **144**, 1188.
- [47] M. R. Palacin, *Chem. Soc. Rev.*, 2009, **38**, 2565
- [48] M. Winter, J.O. Besenhard, M.E. Spahr and P. Novak, *Adv. Mater.*, 1998, **10**, 728.
- [49] R. Kanno, Y. Takeda, T. Ichikawa, K. Nakanishi and O. Yamamoto, *J. Power Sources*, 1989, **26**, 535.
- [50] I. Kuribayashi, M. Yokoyama and M. Yamashita, *J. Power Sources*, 1995, **54**, 1.
- [51] A. Magasinski, P. Dixon, B. Hertzberg, A. Kvit, J. Ayala and G. Yushin, *Nat. Mater.*, 2010, **9**, 353.
- [52] J. Cabana, L. Monconduit, D. Larcher and M. R. Palacin, *Adv. Mater.*, 2010, **22**, E170
- [53] D.C. Marcano, D.V. Kosynkin, J.M. Berlin, A. Sinitskii, Z.Z. Sun, A. Slesarev, L.B. Alemany, W. Lu and J.M. Tour, *ACS Nano*, 2010, **4**, 4806.

- [54] H.L. Wang, J.T. Robinson, G. Diankov and H.J. Dai, *J. Am. Chem. Soc.*, 2010, **132**, 3270.
- [55] P.H. Shi, R.J. Su, F.Z. Wan, M.C. Zhu, D.X. Li and S.H. Xu, *Appl. Catal. B-Environ.* 2012, **123**, 265.
- [56] Y.Y. Liang, Y.G. Li, H.L. Wang, J.G. Zhou, J. Wang, T. Regier and H.J. Dai, *Nat. Mater.*, 2010, **10**, 780.
- [57] S. Woo, J. Lee, S.K. Park, H. Kim, T.D. Chung and Y. Piao, *J. Power Sources*, 2013, **222**, 261.
- [58] L. Li, Z.P. Guo, A.J. Du and H.K. Liu, *J. Mater. Chem.*, 2012, **22**, 3600.
- [59] J.W. Lee, A.S. Hall, J.D. Kim and T.E. Mallouk, *Chem. Mater.*, 2012, **24**, 1158.
- [60] H. Kim, S.W. Kim, J. Hong, Y.U. Park and K. Kang, *J. Mater. Res.*, 2011, **26**, 2665.
- [61] A. Gupta, G. Chen, P. Joshi, S. Tadigadapa and P.C. Eklund, *Nano Lett.*, 2006, **6**, 2667.
- [62] D.H. Long, W. Li, L.C. Ling, J. Miyawaki, I. Mochida and S.H. Yoon, *Langmuir*, 2010, **26**, 16096.
- [63] C.H. Xu, J. Sun and L. Gao, *Nanoscale*, 2012, **4**, 5425.
- [64] C.B. Wang, L.W. Yin, D. Xiang and Y.X. Qi, *ACS Appl. Mater. Interfaces*, 2012, **4**, 1636.

- [65] N. Lavoie, P.R.L. Malenfant, F.M. Courtel, Y. Abu-Lebdeh and I.J. Davidson, *J. Power Sources*, 2012, **213**, 249.
- [66] G.M. Zhou, D.W. Wang, F. Li, L.L. Zhang, N. Li, Z.S. Wu, L. Wen, G.Q. Lu and H.M. Cheng, *Chem. Mater.*, 2010, **22**, 5306.
- [67] D. Li, D.Q. Shi, Z.W. Liu, H.K. Liu and Z.P. Guo, *J. Nanopart. Res.*, 2013, **15**, 1647.
- [68] H.B. Wang, C.J. Zhang, Z.H. Liu, L. Wang, P.X. Han, H.X. Xu, K.J. Zhang, S.M. Dong, J.H. Yao and G.L. Cui, *J. Mater. Chem.*, 2011, **21**, 5430.
- [69] Z.S. Wu, W.C. Ren, L. Xu, F. Li and H.M. Cheng, *ACS Nano*, 2011, **5**, 5463.

초 목

리튬 이온 전지는 전자기기의 주요 동력원으로 사용되어 왔다. 이런 리튬 이온 전지를 전기자동차에 적용하기 위하여 많은 연구가 진행되고 있다. 보다 높은 비용량을 가지고 있으면서 리튬 이온 저장 특성 또한 우수한 새로운 물질의 개발이 요구되고 있다.

본 연구에서는 망간 옥사이드 나노입자의 질소 도핑된 그래핀 화합을 보다 쉬운 수열합성법으로 제조하여 리튬이온 전지 음극소재로서의 향상된 성능을 보여주고 있다. 하이드라진은 여기에서 환원제로 작용할뿐만 아니라 질소 도핑될 수 있는 질소 소스로도 작용한다. 합성된 화합물을 볼 때 평균 사이즈가 20-50 nm 인 망간 옥사이드 나노입자가 질소 도핑된 그래핀의 양쪽 측면에 잘 분산되어 있다. 도핑된 그래핀의 질소함량을 원소분석기로 측정한 결과 질소함량이 2 wt%로 나타났다. 질소 도핑된 그래핀에 담지된 망간 옥사이드 나노입자들은 리튬 이온 전지의 음극물질로 사용하였을 때 뛰어난 전기화학 성능을 보여주었는데 여기에는 높은 가역비용량, 뛰어난 사이클 특성 그리고 훌륭한 출력 특성(2.0 A g⁻¹ 에서 약 400 mA h g⁻¹ 의 용량을 나타냄)을 보여주었다. 이러한

전기화학 특성의 향상은 그래핀에 의한것인데 여기에서 그래핀은 전자 전도체로 작용할뿐만 아니라 부피 완충층으로 작용하였기 때문이다. 질소 도핑을 통하여 에너지 장벽을 낮춤으로써 전자와 이온의 이동속도를 증가시킨 것 또한 전기화학 특성의 향상에 도움을 주었다. 이러한 금속산화물 나노입자와 질소 도핑된 그래핀 화합물은 향상된 특성을 나타내는 리튬 이온 전지의 음극물질로서 유망한 후보라고 할 수 있다.

주요어 : 리튬이온전지, 음극, 망간 옥사이드, 그래핀, 도핑

학 번 : 2012-22575